Research Square

Preprints are preliminary reports that have not undergone peer review.
They should not be considered conclusive, used to inform clinical practice,
or referenced by the media as validated information.

Boundary Condition Characterization for Numerical Simulation of the Flow Inside the Virginia Tech Stability Wind Tunnel

Aurelien Borgoltz

aurelien@vt.edu

Virginia Tech

Nanyaporn Intaratep

Virginia Tech

William Devenport

Virginia Tech

Christopher J. Roy

Virginia Tech

Adwait HogePatil

Virginia Tech

Research Article

Keywords: Wind Tunnel Testing, CFD Validation, Uncertainty Quantification, Boundary Conditions

Posted Date: June 22nd, 2026

DOI: https://doi.org/10.21203/rs.3.rs-9868063/v1

License: This work is licensed under a Creative Commons Attribution 4.0 International License.
Read Full License

Additional Declarations: No competing interests reported.

Boundary Condition Characterization for Numerical Simulation of the Flow Inside the Virginia Tech Stability Wind Tunnel

Aurelien Borgoltz[1*], Nanyaporn Intaratep[1†], William Devenport[1†], Christopher J. Roy[1†], Adwait HogePatil[1†]

[1*]Kevin T. Crofton Department of Aerospace and Ocean Engineering , Virginia Tech, 660 McBryde Hall, 225 Stanger Street t, Blacksburg, 24061-0119 , VA, USA.

*Corresponding author(s). E-mail(s): aurelien@vt.edu;
Contributing authors: nintarat@vt.edu; wdevenpo@vt.edu; cjroy@vt.edu; adwait@vt.edu;
†These authors contributed equally to this work.

Abstract

The aerodynamic and geometric boundary conditions of the highspeed leg (including the settling chamber, the contraction, and the test-section) of the Virginia Tech Stability Wind Tunnel (VTSWT) have been documented in detail to provide a validation data set for numerical simulations of the flow inside the facility as part of the NATO STO activity AVT-387 Common Research Wind and Water Tunnels for CFD Verification and Validation. In particular, this paper shows detailed measurements of the flow in the settling chamber, over the full cross-section downstream of the last turbulence screen (5.5m×5.5m). The mean surface pressure distribution on the 4 walls in the contraction liner (covering the latter half of the contraction) and the two side walls in the test-section has been documented, along with the shape and growth of the boundary layer across all 4 walls and along the entire test-section. The details of the corner flow at the nominal model testing location were revealed by stagnation pressure contours and have proven important for evaluating the accuracy of the numerical simulations. Finally, the as-built geometry was extracted from multiple scans of the facility and an idealized cross-section data set, smooth enough to allow for efficient yet accurate CFD meshing, was generated by assuming sharp corners at the wind tunnel wall intersections.

Keywords: Wind Tunnel Testing, CFD Validation, Uncertainty Quantification, Boundary Conditions

1 Introduction

Computational Fluid Dynamics (CFD) provides practical means for the prediction of many marine and aerospace vehicle flows. The potential value of accurate CFD models is huge, not just in the design and development of new vehicles and the cost and time savings that would be achieved by reducing the burden of experimental testing, but also in real-time predictions of their performance, in maneuvering and operations. Unfortunately, CFD models have not yet achieved this level of accuracy, particularly with respect to separated flows, corner flows and complex surfaces such as roughness. Improving models requires comparison with measurements, usually involving testing campaigns in wind or water tunnel facilities. Traditionally, such campaigns involve the testing of a model or component in a wind tunnel test-section with the intent of simulating the 'free-flight' conditions, i.e., the idealized state of immersing the device in an otherwise uniform stream of infinite extent. This idealized condition is then simulated using CFD. The problem here, of course, is that this ideal state is rarely achieved. Regardless of how well the experiment is designed, the wind tunnel flow has different boundary conditions than free flight and the effects of its more constrained boundaries and nonuniformities can have a significant influence on the fluid dynamics of the devices. The standard approach for dealing with this problem is to use simplified methods to establish wind tunnel 'corrections' (formulae usually based on linearized inviscid analysis) to factor out the confining effects of the wind tunnel boundaries.

However, the uncertainties in the CFD models are now on par with those in wind tunnel corrections and in the boundary conditions they assume. It is therefore required, to enable accurate CFD, to replicate as closely as possible the actual inflow and boundary conditions of wind tunnel tests. Doing so requires detailed and thorough documentation of the aerodynamic and geometric boundary conditions inside testing facilities. The purpose of the NATO STO activity AVT-387 Common Research Wind Tunnels (CRWTs) is therefore to determine which features (and what level of fidelity) of the testing facilities need to be included in the CFD modelling to obtain accurate simulation of the flows they generate. This paper is therefore aimed at presenting a detailed and comprehensive overview of the work that has been undertaken at the Virginia Tech Stability Wind Tunnel (VTSWT) to document such boundary conditions.

2 Facility and Instrumentation

2.1 The Virginia Tech Stability Wind Tunnel

The VTSWT is a continuous, single return, subsonic wind tunnel with 7.32m long removable rectangular test-sections of square cross section, nominally 1.85m on edge. The general layout is shown in Fig.1. The tunnel is powered by a 0.5MW variable

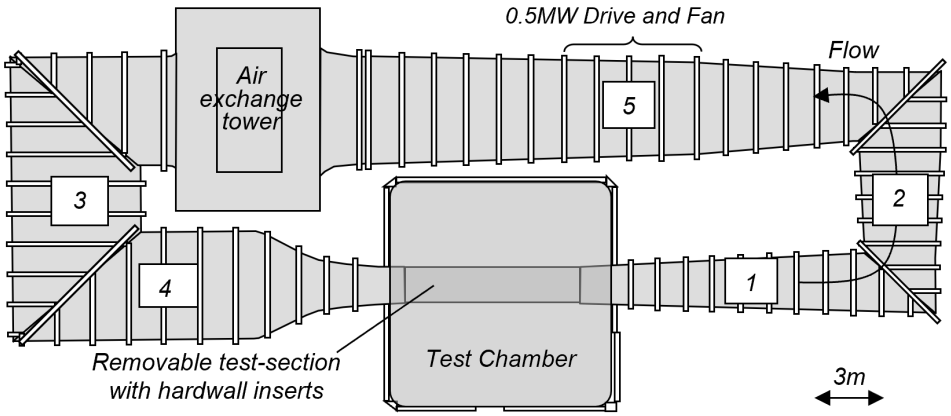


Fig. 1: Top view schematic of the Virginia Tech Stability Wind Tunnel in aerodynamic configuration.

speed DC motor driving a 4.3m-diameter propeller at up to 600 RPM. This provides a maximum speed in the test-section (with no blockage) of about 80m/s and a Reynolds number per meter up to about 5,000,000. A variable thickness machined-Delrin liner is used around the fan to generate a constant tip gap 8.9±0.8mm. The tunnel forms a closed loop, but has an air exchange tower open to the atmosphere to allow for temperature stabilization. The air exchange tower is located downstream of the fan and motor assemblies. Downstream of the tower, the flow is directed into a 5.5m×5.5m settling chamber containing 7 turbulence-reducing screens each with an open area ratio of 0.6 and separated by 0.15m. Flow exits this chamber through the 9:1 contraction nozzle, which further reduces turbulence levels and accelerates the flow to test speed. The walls of the downstream half of the contraction were recently upgraded [1] to provide a smooth surface (made of curved aluminum panels) instrumented with 64 pressure taps (16 on each wall), seen in Fig.2. To ensure uniformity of the flow on all four walls a 3.2mm-thick serrated metal strip is applied on all 4 walls, at 3.57m upstream of the test-section entrance (the leading edge of panel P1 as shown in Fig.3). The corners of the contraction liner are sealed with white polyurethane sealant (that can be seen in Fig.2) resulting in fillets with a radius of approximately 12.7mm.

At the downstream end of the test-section flow passes into a 3-degree diffuser. Eight 0.16m-high vortex generators located 0.78m from each corner around the floor, walls and ceiling of the flow path at the entrance to the diffuser serve to mix momentum into the diffuser boundary layer, minimizing the possibility of separation and the consequent instability and inefficiency. The four corners in the flow path (two between the air exchange tower and settling chamber, and two between diffuser and fan) are equipped with diagonal arrays of shaped turning vanes with circular arc profiles. Spacing between the vanes is 0.3m except in the corner immediately ahead of the settling chamber where the spacing is 0.076m. The VTSWT has interchangeable aerodynamic and anechoic configurations. Both configurations use the same test-section, the difference residing in the type of side walls and panelling used. In anechoic configuration,

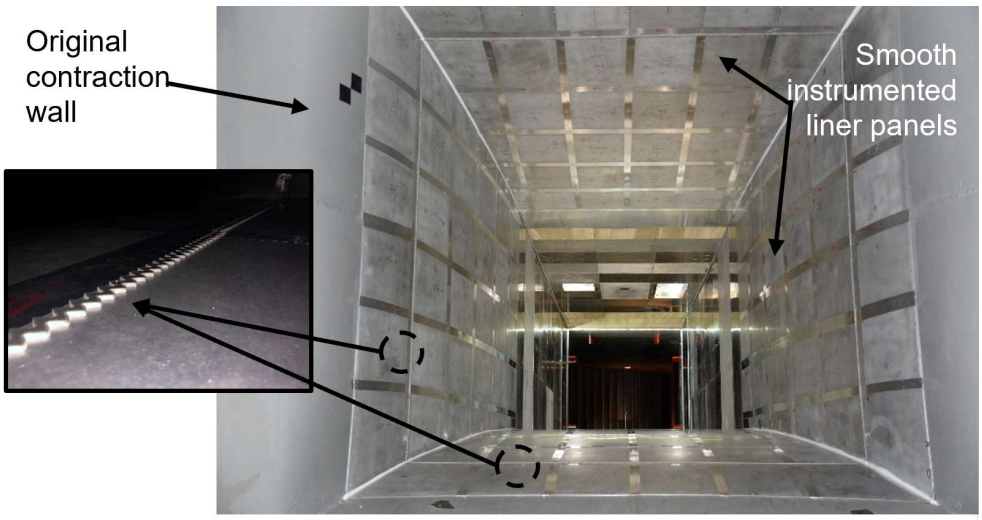


Fig. 2: Instrumented contraction liner (seen from upstream, flow into the page) with details of the 3.2mm-thick serrated trip strip in the contraction of the VTSWT.

the sidewalls are made of stretched Kevlar fabric (to allow sound from the test-section to escape and be absorbed by external acoustic treatment), and the floor and ceiling panelling consists of perforated metal panel covered with Kevlar fabric. The experimental effort detailed in this publication focused on the aerodynamic, or "hardwall", configuration. In this setup, the sidewalls are made of an aluminium reinforced frame into which solid modular 0.61m×0.61m aluminum panels are installed (see Fig.4). These panels have the same exact size as the floor and ceiling panels. The aerodynamic configuration offers several major advantages as the hard walls are extremely versatile, allowing the installation of a variety of modular custom instrumentation setups based on the 0.61m panelling (that can be mounted on any of the four walls). The labelling of the different streamwise stations associated with each row of aluminum panels (P1 through P9) are indicated on Fig. 3, along with the origin of the streamwise coordinate in the test-section coordinate system (shown in red in Fig. 3). All the panels are identical and measure 0.61m streamwise, except for the P2 row of panels that are 0.565m.

In Fall 2023, it was discovered that the method of mounting the hard walls led to a slight faring angle (less than 0.1°). This angle was eliminated in late 2023 and early 2024 when the hardwall mounting and positioning method was corrected. This correction led to the need to obtain a new optical scan and new boundary condition testing campaign in February 2024 (following the initial effort in 2022 and 2023 [2]).

Acoustic treatment is present on the walls of the circuit in the flow path and includes a 25-mm to 50-mm thick melamine foam liner used to treat the side walls and ceiling of the diffuser, a 50-mm thick melamine foam liner on the walls and ceiling of the south leg of the tunnel (section 2 in Fig. 1), a 50mm melamine foam liner on the

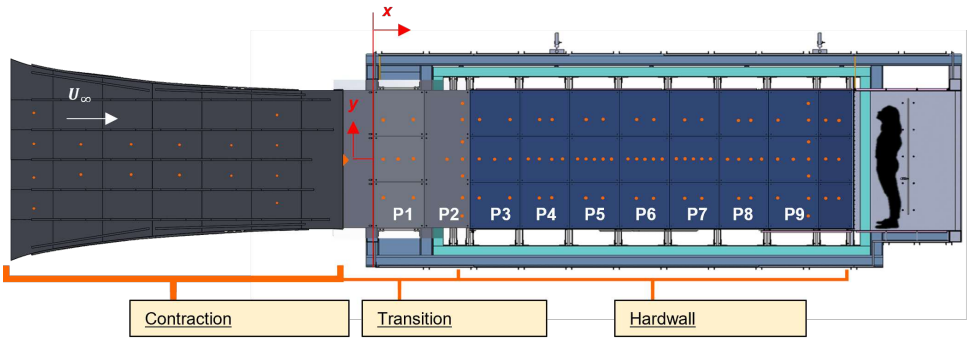


Fig. 3: Side view of the VTSWT (seen from behind the port wall) contraction and test-section fitted with the hardwall configuration of the anechoic test-section. Orange dots indicate the position of mean pressure taps. Adapted from Vishwanathan et. al [1]

side walls and floor of the north leg of the tunnel (section 3), as well as on the side walls of the portion of the settling chamber upstream of the screens (section 4).

The test-section itself is located in a hermetically sealed steel test chamber (Fig. 1). The pressure inside this control room is equalized with the static pressure in the test-section flow, this being below atmospheric by an amount roughly equal to the dynamic pressure. Pressure is equalized through a metered nozzle, located at the start of the diffuser on the port wall, and designed to minimize parasitic noise. To prevent leaks between the test-section and test chamber, cylindrical 15mm-diameter rubber gaskets are placed in the corners of the test-section along its entire length (as seen in Fig. 4).

The core flow through the empty test-section (measured with a hard-wall test-section in place) is both closely uniform and of very low turbulence intensity. Measurements of freestream turbulence levels as a function of flow speed (performed in 2021) have shown turbulence levels (given in Table. 1) as low as 0.010% at 20m/s and increasing gradually with flow speed (up to 0.023% at 70m/s).

Table 1: Variation of freestream turbulence intensity at the center of the test-section in the VTSWT.

Freestream Velocity U_∞ [m/s]	Freestream Turbulence Intensity $\%U_\infty$
20.06	0.0102
30.09	0.0101
40.07	0.0136
50.01	0.0151
59.98	0.0186
70.17	0.0230

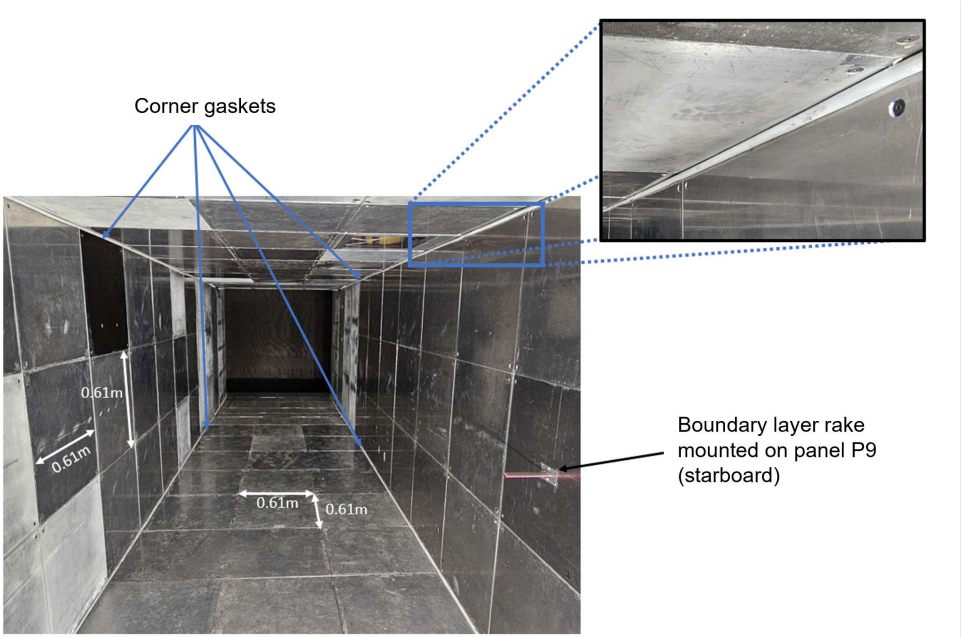
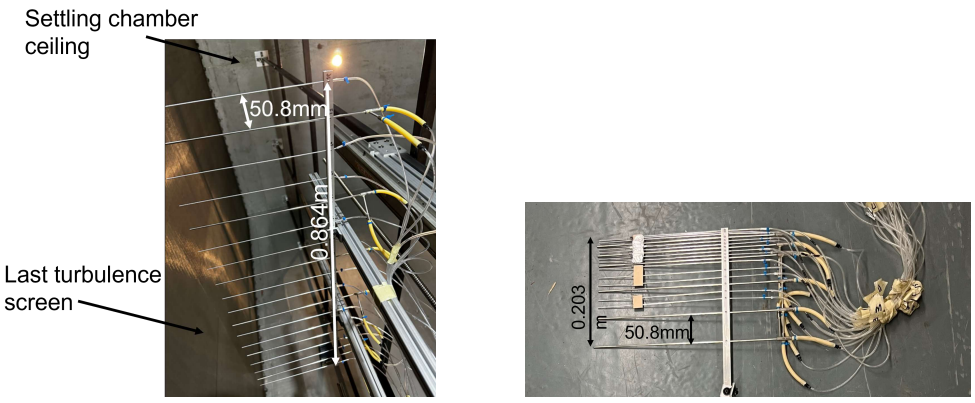


Fig. 4: View of the empty aerodynamic test-section (looking upstream) featuring the 0.61m-panelling, boundary layer rake, and corner gaskets.

2.2 Reference Conditions Locations and Measurements

The reference flow speed in the test-section U_∞ is defined as the velocity at the center of the test-section. Until 2025 [3], the reference location for this velocity was set 3.502m downstream of the entrance of the test-section, at the midpoint between the two side walls, and 0.313m off the floor. Following analysis of the decay of the pressure disturbances generated by the paneling in the test-section, derived from CFD results of the as-built geometry, the location (and associated calibration) of the reference velocity was moved to 0.61m off the floor. During tests, the reference velocity is monitored using the pressure difference between 2 static pressure taps located on the side walls of the wind tunnel settling chamber (7.904m upstream of the test section entrance and 0.166m below midspan) and 6 taps located in the contraction liner (2.085m upstream of the start of the test-section) on the port, ceiling, and starboard walls (0.1m above and below the wall centerline). These pressures are sensed using a Datametrics Barocel Pressure Sensor Type 590D with traceable calibration, and recorded using a TE ESP32HD DTC miniature pressure scanner (controlled by a DTC Initium unit) with a range of $\pm$20inWC and a rated accuracy of 0.05% F.S. The reference pressure difference is calibrated against the readings of a Pitot-static probe located at the reference location mentioned above. Once the calibration has been performed (at least once a year, or after any test-section configuration change), the reference Pitot-static probe is removed and the calibration is applied to the settling chamber and contraction pressure readings to set the tunnel reference conditions. Temperature in the test-section



(a) (b)

Fig. 5: Details of inflow rakes: (a) main rake mounted in the settling chamber and (b) logarithmic rake outside of the wind tunnel used for measuring the settling chamber inflow.

is monitored using an Omega Thermistor type 44004 (accuracy ±0.2°C) located on the port wall at the start of the diffuser (0.4m downstream of the test-section exit, or 7.72m downstream of the inlet of the test-section). The ambient absolute pressure in the test chamber is determined using an Omega MMB26 series high accuracy absolute pressure transducer (with a range of 880-1084mbar, and a rated accuracy of ±0.05%).

2.3 Settling Chamber Inflow Rakes and Traversing

Measuring the inflow to the highspeed leg required mapping out the stagnation and static pressures 0.33m downstream of the last turbulence screen, in the settling chamber. Due to the 9:1 contraction ratio, the settling chamber features a large area that is nominally 5.5m × 5.5m. Such measurement required the fabrication of 2 custom rakes and associated traversing system. While both rakes feature 18 straight probes (12 stagnation probes and 6 Pitot-static probes), 3.18mm in diameter, the main rake had them evenly distributed (every 50.8mm) over a length of 0.864m. This rake was used for all the measurements away from the port and starboard side walls. To provide better measurement resolution closer to those walls, a second rake was built, using the same 18 probes described above but arranged in a logarithmic distribution over a length of 203mm. The location and position of each probe in the 2 rakes is provided in Table 2 and shown in Fig. 5.

The rakes were in turn mounted on screw-driven linear carriage actuators, 2m in length. The actuators were mounted on a support steel beam structure (shown in Fig. 6). This structure, installed only for the inflow cross-section measurement, is removable and can be completely disassembled, including the mounting bracket that bolt to each wall for stability, leaving little to no surface defects on the settling chamber walls. When in use, the actuators are mounted vertically between two beams of the structure and can be manually positioned across the entire cross-section (covering approximately

Table 2: Position and type of probes used in the (a) logarithmic rake and (b) main rake.

(a)				(b)		
Channel	Position (mm)	Type		Channel	Position (mm)	Type
1	3.2	Total		1	12.7	Total
2	6.4	Total		2	63.5	Pitot-Static
3	9.5	Total		3	114.3	Total
4	15.9	Pitot-Static		4	165.1	Total
5	22.2	Total		5	215.9	Pitot-Static
6	28.6	Total		6	266.7	Total
7	34.9	Pitot-Static		7	317.5	Total
8	41.3	Total		8	368.3	Pitot-Static
9	47.6	Total		9	419.1	Total
10	54	Pitot-Static		10	469.9	Total
11	60.3	Total		11	520.7	Pitot-Static
12	76.2	Total		12	571.5	Total
13	88.9	Total		13	622.3	Total
14	101.6	Pitot-Static		14	673.1	Pitot-Static
15	114.3	Total		15	723.9	Total
16	127.0	Total		16	774.7	Total
17	152.4	Pitot-Static		17	825.5	Pitot-Static
18	203.2	Pitot-Static		18	876.3	Total

97.8%). For the remaining 2.2%, the logarithmic rake is used (as shown in the red shaded areas in Fig. 6).

The pressures from the rakes were measured using Setra Model 264 pressure transducers (with a rated accuracy of ±0.25%F.S) with 0.5inWC range for the static pressures and 1.5inWC range for the stagnation pressure channels. The signal from the pressure transducers were acquired with a National Instrument NI-9220 module running in a cDAQ-9189 control frame.

2.4 Boundary Layer Rake

2.4.1 Wall Boundary Layer

Boundary layer profiles are measured with a boundary layer rake, made of 3D-printed metal by Vectoflow GmbH. This rake is 154.2mm tall, 62.5mm in chord. The body, shaped like a symmetrical airfoil to minimize the blockage effects, is 42.5mm in chord with the tip of the probe extending 20mm upstream of it. The rake features 30 total pressure probes distributed in a semi-logarithmic spacing. Due to the physical constraints of the 1mm-diameter total pressure tubes, the first 11 tubes are evenly spaced over the first 10.5mm from the base of the rake. The 19 tubes above 10.5mm are logarithmically spaced. The probe tip coordinates y_w, measured from the base plate of the rake, are provided in Table. 3 and Fig. 7. Note that for accuracy, the exact position of the rake probes is measured once it is installed in its panel, and one may accordingly see small variations in the coordinates provided below.

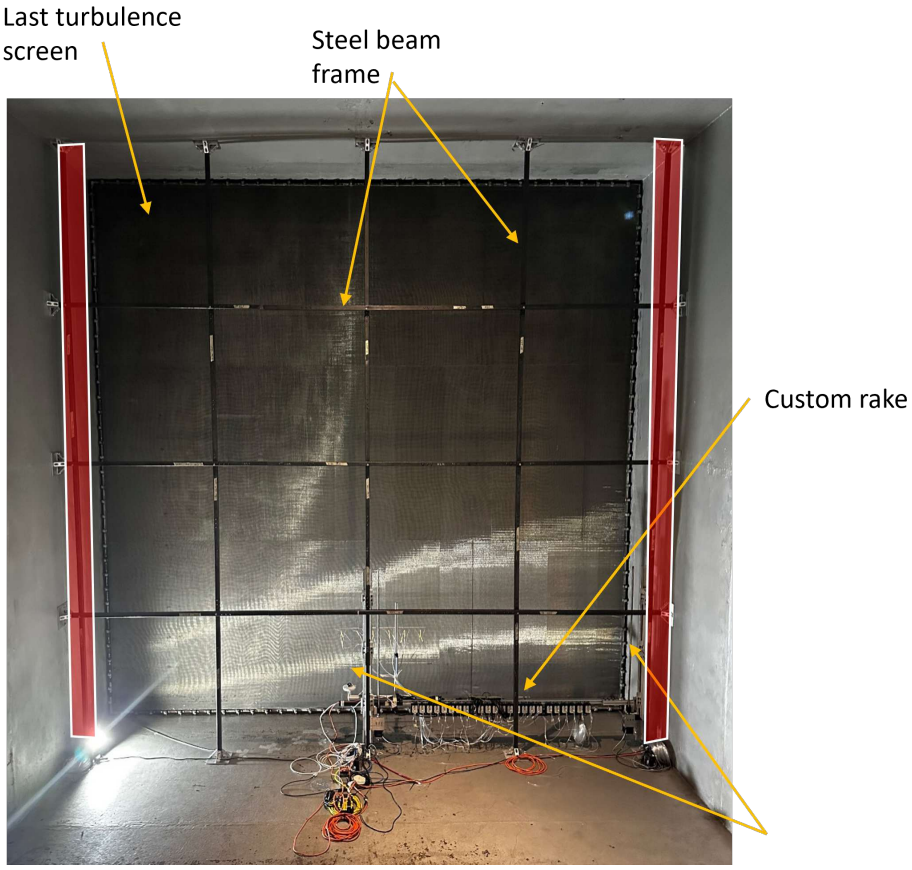
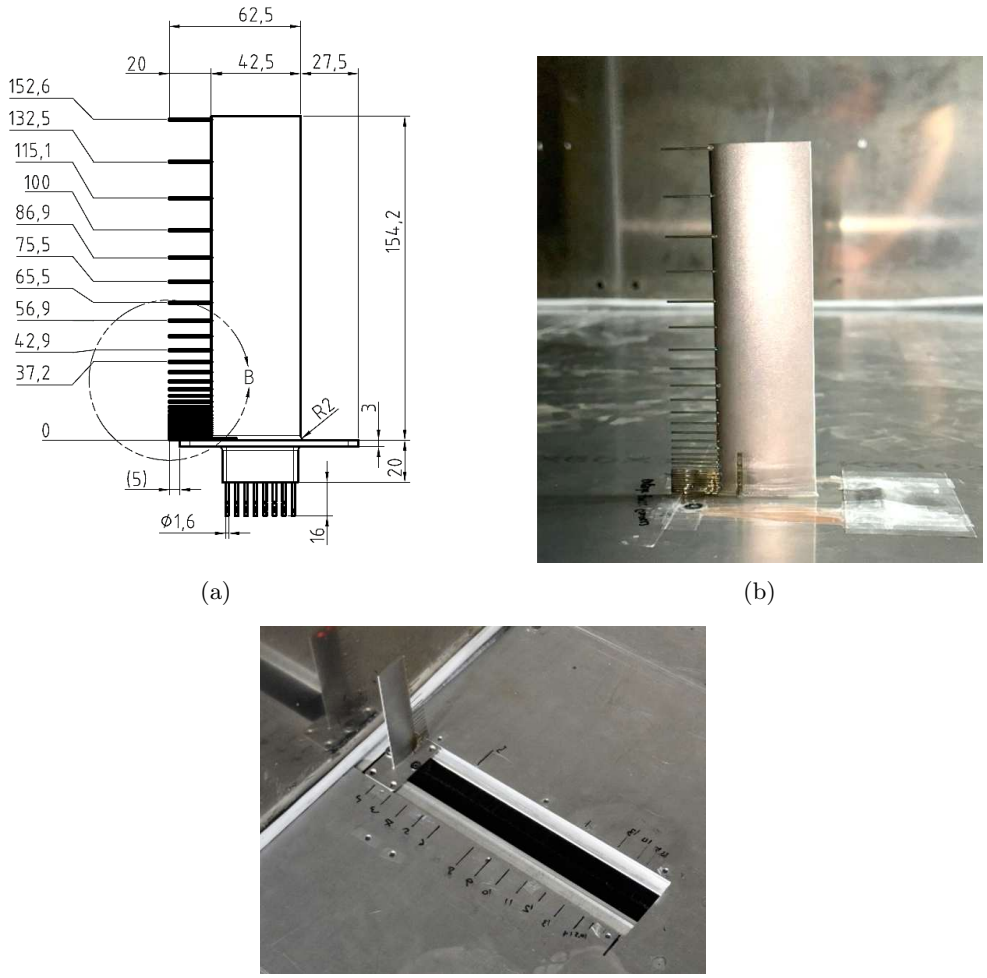


Fig. 6: Inflow rake and support structure mounted in the VTSWT settling chamber. The regions where the logarithmic rake was used is shown in the red shaded area.

Table 3: Boundary Layer Rake Probe Coordinates (where y_w is zero at the base of the rake).

Port	y_w (mm)	Port	y_w (mm)	Port	y_w (mm)
1	0.5	11	10.5	21	42.9
2	1.5	12	11.9	22	49.4
3	2.5	13	13.8	23	56.9
4	3.5	14	15.9	24	65.5
5	4.5	15	18.3	25	75.5
6	5.5	16	21.1	26	86.9
7	6.5	17	24	27	100
8	7.5	18	28.1	28	115.1
9	8.5	19	32.3	29	132.5
10	9.5	20	37.2	30	152.6



(a) (b)

(c)

Fig. 7: Details of the boundary layer rake: (a) side view drawing with detailed dimensions, (b) side view of the rake mounted on the wall of the VTSWT, and (c) downstream view of the rake mounted on the floor of VTSWT near the port side.

The rake was 3D printed using stainless steel to maximize the number of internal passages, channels cut inside the main body of the rake going from the probes to the tubing connector base seen at the bottom of Fig. 7a. This fabrication method makes for a robust and self-contained system that can be bolted to a 0.61m×0.61m wall panel using 4 countersunk screws in the base plate of the rake. This aluminum panel features 2 static pressure ports that can be used to determine the local static pressure at the rake location.

The pressure lines from the 30 rake ports and the 2 static ports are connected to a DTC Initium ESP32HD miniature pressure scanner (with a $\pm 20 inWC$ range and rated accuracy of $\pm 0.05\%$ full scale). The scanner is mounted directly on the rake panel, allowing the entire assembly to be efficiently relocated on either of the side walls, floor, or ceiling, and such that the tip of the probes is near the center of the panel.

2.4.2 Test-Section Corner Flow

To characterise the flow field at the 4 corners of the test-section where the boundary layers of each wall intersect, a boundary layer rake was installed over a panel with a single-axis linear traversing system attached (Fig. 7b). At a fixed streamwise location, the rake can then move in spanwise and transverse direction in controllable increments, enabling a quick survey of boundary layer profiles at multiple points close to the corners. This traversing rake, used for the corner flow investigation, features a 393.7mm-long slot sealed with nylon brush strip. Three static pressure taps were instrumented directly on the panel itself upstream of the traversing slot for dynamic pressure calculation. The linear traversing system, located on the side of the panel outside of the test-section, is based on a Velmex BiSlide model MN10-0150-E01-21. Two measurements were required to reconstruct the full cross-section of the flow in a given corner. The resulting data were 2-D interpolated to achieve a nominal 0.35m by 0.35m cross-section of velocity magnitude. This corresponds to 20% of the test-section width

2.5 Optical CMM Scanners

One significant goal of the AVT-387 activity is to determine the minimum level of fidelity required to produce accurate simulation of the flow inside the VTSWT. Doing so obviously requires detailed characterization of the aerodynamic boundary conditions alluded to above as well as detailed documentation of the physical boundary condition of the computational domain: the actual shape of the circuit walls. Due to the large contraction ratio of this subsonic wind tunnel, the cross-section of the VTSWT varies from 1.85m $\times$ 1.85m in the test-section to 5.5m $\times$ 5.5m in the settling chamber. Therefore, two different optical coordinate-measuring machines (CMM) were combined to obtain the full scan of the tunnel highspeed leg (settling chamber + contraction + test-section). In the test-section, a high accuracy CREAFORM MetraScan 3D Black Elite scanner was used. In the settling chamber and first half of the contraction, where the overall dimensions along with the sloping of the walls are not conducive to using handheld devices, a longer-range FARO Focus 3D scanner was used instead.

2.5.1 FARO Focus 3D

The scan of the circuit using the FARO Focus CMM was performed in 2019 after the installation of the contraction liner detailed in [1]. The scan provides cloud point information from the outlet of the last turbulence screen in the settling chamber to the first set of turning vanes at the exit of the highspeed diffuser. With a rated accuracy of 1mm, the FARO Focus 3D scanner is a LiDAR system designed to scan large volumes. However, the 1mm rated accuracy of the scanner being a couple orders of magnitude lower than the Metrascan 3D (described in the next section), it was

decided to rely on the FARO Focus 3D CMM only in the areas the Metrascan could not reach (i.e. the settling chamber and the first half of the contraction, up to the start of the contraction liner). During the processing of the as-built geometry, the uncertainty in the geometry extracted from the FARO point cloud was found to be typically within $\pm 2mm$. However, it was also discovered that the FARO point cloud tends to show increased levels of noise in the corners furthest from the scanner. In our case, the scanner was positioned on the floor of the tunnel circuit approximately along the centerline. Consequently, the ceiling corners in the settling chamber featured significantly higher variations than the rest of the domain, on the order of $\pm 5mm$ or greater. The exact source of this increased uncertainty has not been identified, but seems to arise when a combination of distance to the target (4-5m) and incidence of the laser light (45-60deg) occurred. The processes used to address this noise in the point cloud processing are detailed in 3.6.

2.5.2 MetraScan 3D

The CREAFORM Metrascan 3D was used to obtain the as-built geometry in the contraction liner and in the test-section. The Metrascan system features a handheld LiDAR unit with two cameras and a lasing unit. The handheld unit position in space is tracked through a second set of two fixed cameras mounted on a tripod called C-Track. The C-Track captures the location of the handheld unit as well as fixed reference reflective targets that can be positioned throughout the measurement volume. These targets provide a fixed reference to establish the global coordinate system for each scan. The combination of the two technologies results in very high accuracy (the system is rated at 0.025mm) over a large measurement volume (9.1m^3). The measurement volume (combining the contraction liner and test-section, for a total of approximately 46m^3) was broken down in 8 scans, for a total of 23 million points. The mesh resolution (the triangle size in the output mesh) was set at 4mm. This value was chosen as an optimum between scanning fidelity and managing the computer resources needed to handle the large number of points generated. Typical variations in the Metrascan point clouds were on the order of $\pm 0.05mm$ in regions of low curvature and up to $\pm 0.3mm$ in higher curvature regions (like the contraction liner).

3 Characterization of Experimental Boundary Conditions

The highspeed leg of the circuit (settling chamber + contraction + test-section) was chosen as the focus of the AVT-387 in the VTSWT. As discussed in the accompanying computational effort paper by Roy *et. al.* [4], the flow in the highspeed diffuser was not simulated in the empty test-section validation case as it was shown to be of minimal impact on the flow inside the test-section (beyond 1m upstream of the test-section outlet). As such, the bulk of the experimental efforts (and indeed the computational domain itself) have focused on the part of the circuit from the exit of the last turbulence screen (settling chamber) to the exit of the test-section. Measurements included both aerodynamic and geometric quantities, such as:

- pressure at the inlet of the domain
- mean wall pressure in the latter half of the contraction (on all 4 walls) and on the port and starboard walls in the test-section
- stagnation pressure profiles of the boundary layers on all 4 walls of the test-section
- stagnation pressure cross-section of the flow in the 4 corners of the test-section
- in-flow pressure gradient on the centreline just above the floor wall
- the actual shape of the highspeed leg of the circuit (the geometric boundary condition, obtained through LiDAR measurements)

These measurements are detailed in sections below. Note that all the aerodynamic measurements were acquired at a minimum of 3 nominal reference Reynolds number of 1.7, 2.8, 3.9M per meter, unless specified. This paper will focus on presenting these data at Re=2.8M/m.

3.1 Inflow Cross-Section

The inflow cross-section data is the only aerodynamic data that was acquired at a single Reynolds number (2.8 million per meter) due to the logistical burden associated with the measurement. The inflow cross section data, measured downstream of the turbulence screens using stagnation and Pitot-static probes (2.3), are interpolated and plotted as velocity contours (in m/s) shown in Fig. 8. The boundaries of the cross-sectional plot match the nominal settling chamber walls as viewed from upstream, where the port side is located on the right side of the plot. The contours show closely uniform inflow in the potential core of the settling chamber where the velocity magnitude varies between 4 and 5 m/s. Near each of the 4 walls, the velocity increases from the core flow due to the framing structure of the turbulence screens. The screen framing leaves approximately 50-mm gaps between the edges of the screens and each wall, resulting in local surge in velocity magnitude up to 12 m/s as a jet is formed due to the lower blockage. When closely observing the flow field near the wall and corner sections (as shown in Fig. 9), the contours indicate some nonuniformity and asymmetry in the flow field near the wall. Low momentum flow regions located next to the high momentum jet regions can also be found near both bottom corners of the figure. The locations of both features likely have an impact on the boundary layer as it progresses into the test-section.

3.2 Contraction and Test-Section Wall Pressures

The wall boundary conditions for CFD validations are presented as the mean pressure coefficient distribution, C_p, along the centerline of the contraction and test-section walls. While the flow in the VTSWT is subsonic, with the maximum Mach number of 0.25 at sea level condition, the calculation of C_p and velocities associated to the aerodynamic boundary conditions in the contraction and test section were performed using isentropic relations for direct comparison to compressible CFD solvers. The measurements were performed on all four walls in the contraction (starboard, port, ceiling and floor) and on the two side walls for the test section (starboard and port). As seen in Fig. 10, there are small variations between the pressure distribution on each wall, both in the contraction and test-section, at a Reynolds numbers of 2.8 million per

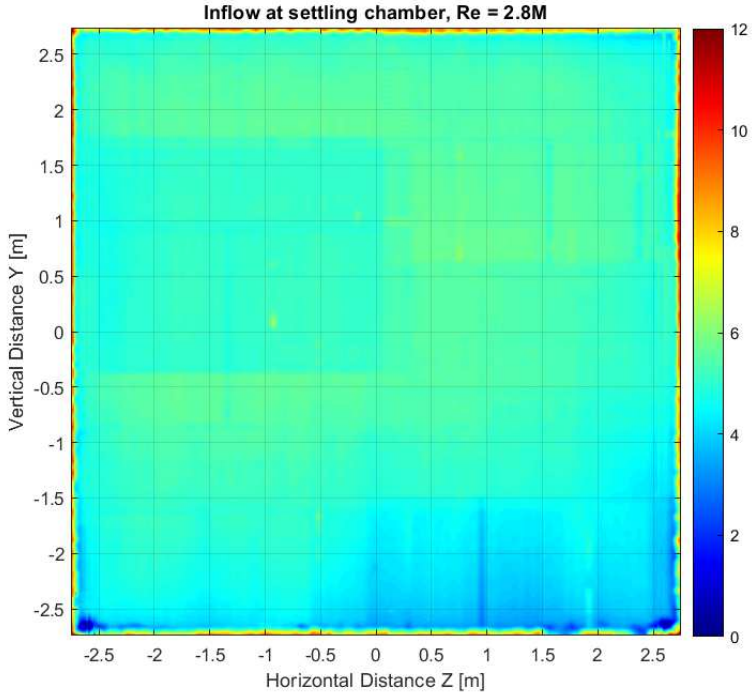


Fig. 8: The inflow velocity cross section (in m/s) at the entrance of the settling chamber for the reference Reynolds number of 2.8 million per meter.

meter. The contraction, having large streamwise pressure gradient, indicates significant flow acceleration as expected, with the flow entering the test-section with consistent C_p values on all four walls. In the test-section (starting at x = 0m), a noticeable deviation in the pressure coefficient between the two walls illustrate the local impact of the wall surface on the wall pressure coefficients. However, the flow can be seen to exit the test section at nearly identical wall pressure levels. While differences can be seen between the two walls, the overarching pressure gradient appears to be consistent, suggesting that the variations may be due to either the wall panelling or the individual quality of the pressure taps. This local variation could have an impact if freestream conditions are based on wall pressures as it is a common practice to define a reference flow condition based on wall pressure at a specific location.

3.3 Test-Section Boundary Layer Profiles

In addition to the wall pressure distribution, the wall boundary conditions were further characterized by investigating the velocity profiles on the test-section wall boundary layers, as stated in 2.4.1. Fig. 11 presents the profiles for the Reynolds number of 2.8 million per meter at x = 1.431m (a) and 3.260m (b) on all four walls, at the centreline of each wall, along with the profile obtained by averaging all four walls.

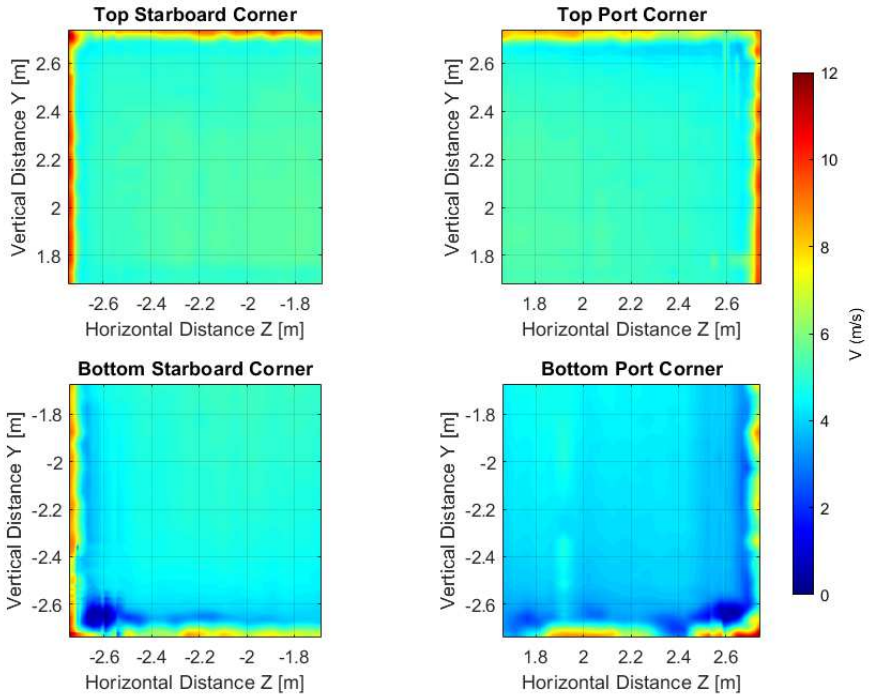
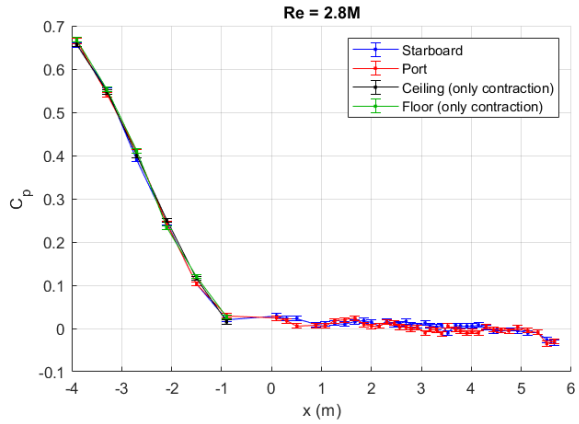


Fig. 9: Focus on the details of the inflow velocity cross section in the 4 corners of the settling chamber for the reference Reynolds number of 2.8 million per meter. Each plot represents a 1.1m × 1.1m region.

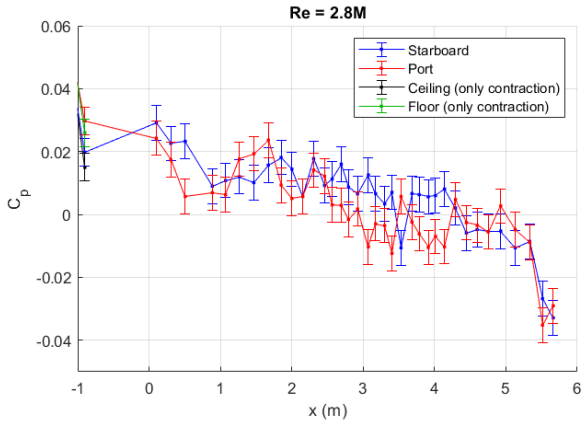
The first streamwise location is near the test-section entrance and the variation in the profile shape between walls are smaller than those found at the second location which is 0.242m upstream of the reference location, implying that the boundary layers coming out of the contraction is quite uniform. The difference seen in Fig. 11b suggests that each wall experiences different boundary growth, likely highlighting the impact of the wall panelling (edges and bowing) that will be presented in 3.6 The boundary layer thickness and associated integrated quantities, momentum and displacement thicknesses, for 7 streamwise locations on each wall are presented in Fig. 12, along with their associated wall-averaged value. The streamwise variation shows that the floor produces the thickest boundary layer and most rapid growth.

3.4 Corner Flow Cross-Sections

The same instrumentation used to document the wall boundary layer on the centerline of each wall, the flow field in the test-section corners was also investigated using measurements of boundary layer cross-sections at x = 3.260m. The profiles accumulated for the two joining walls of a given corner were interpolated to achieve velocity magnitude contours of the corner flow. Fig. 13 presents normalized velocity magnitude



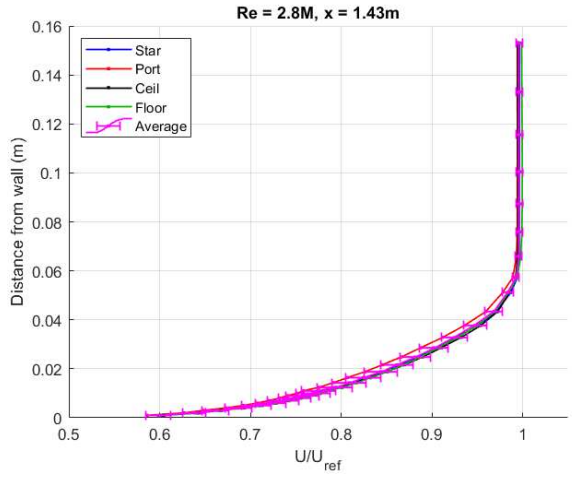
(a)



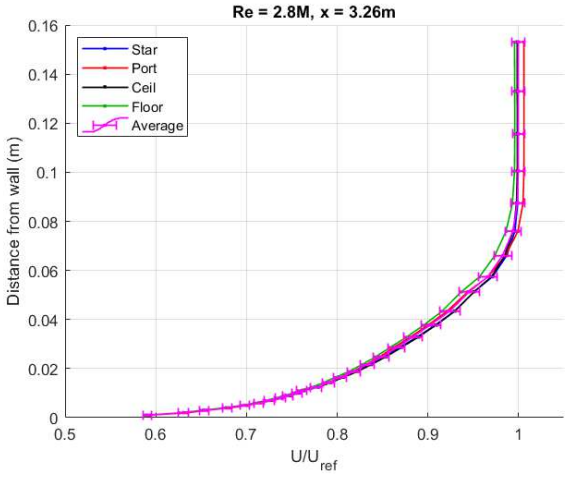
(b)

Fig. 10: Pressure coefficient distributions at Reynolds number of 2.8 million per meter along the centerline of the tunnel walls of (a) the contraction and test-section, (b) focusing on the test-section only.

(V/U_{ref}) contours in each corner of the test-section as seen looking from upstream (the left side of the plot representing the starboard wall). The corner flow does not present similar flow pattern between all four corners. The bottom corners have thicker boundary layers, consistent with the results seen in the inflow cross-section in 3.1. Furthermore, the flow in the corner itself appears noticeably different between the two bottom corners and the two top corners, with indication of different magnitude



(a)



(b)

Fig. 11: Boundary layer velocity profiles at Reynolds number of 2.8 million per meter on the test-section walls at a) xx_s=1.431m and b) x_s=3.260m. The average value for each quantity is provided along with the associated experimental uncertainty.

of secondary flow patterns between the top and bottom corners. Fig. 14 shows the normalized velocity contours averaged across the four walls and presented as the bottom port side corner (this is done to simplify the comparison with the as-designed computations discussed in [4])

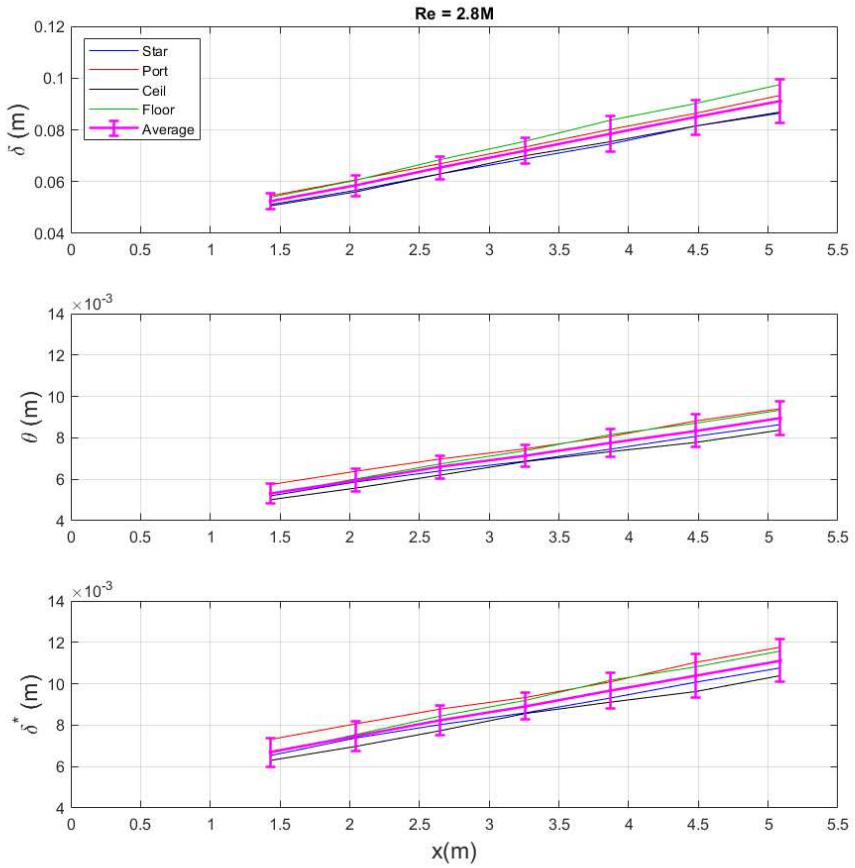


Fig. 12: Boundary layer overall thickness, momentum thickness, and displacement thickness variation with streamwise location for all test-section walls at Reynolds number of 2.8 million per meter. The average value for each quantity is provided along with the associated experimental uncertainty.

3.5 Uncertainty Analysis

The uncertainty analysis of the measurement quantities were adapted from the procedure developed for model validation by Rhode and Oberkampf [5] and recently implemented in the VTSWT by Duetsch-Patel [6]. The uncertainties were characterized through 3 contributions, random (δ_{rand}), flow-field nonuniformity ($\delta_{flowfield}$), and model geometry/instrumentation (δ_{instr}), as listed in Eq. 1 for the total uncertainty (δ_{total}).

$$\delta_{total} = \delta_{rand}^2 + \delta_{flowfield}^2 + \delta_{instr}^2 \tag{1}$$

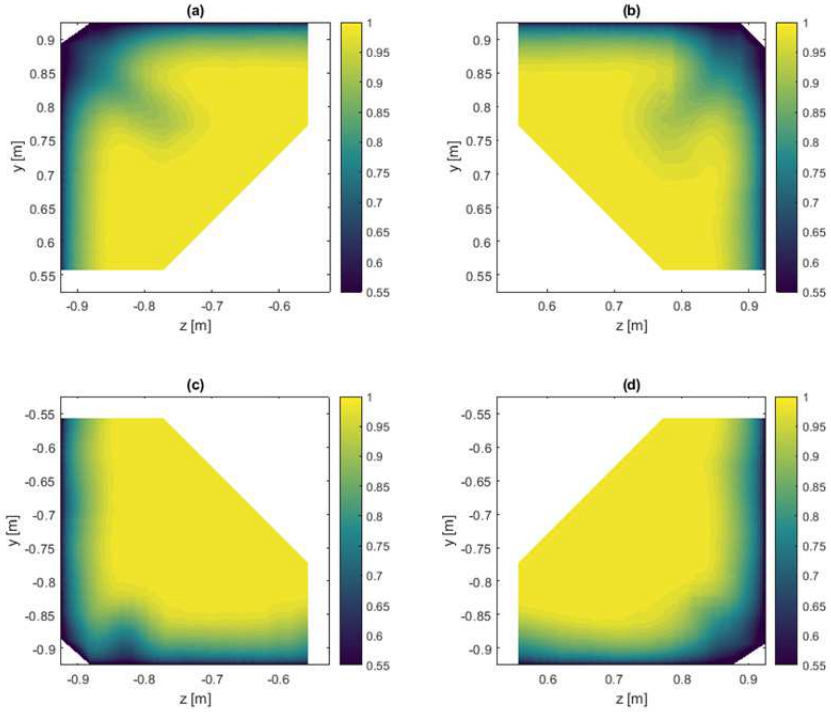


Fig. 13: Velocity ratio (V/U_{ref}) contours of the corner flows at Reynolds number of 2.8 million per meter in the test-section at a streamwise location of 3.260m for (a) the starboard-ceiling corner, (b) the port-ceiling corner, (c) the starboard-floor corner, and (d) the port-floor corner.

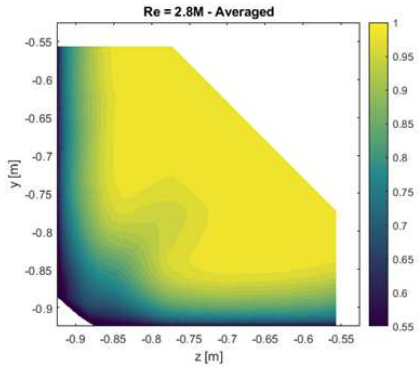


Fig. 14: Wall-averaged contours of the normalized velocity from all four walls at a streamwise location of 3.260m (Reynolds number of 2.8 million per meter) and plotted as a bottom port side corner.

The random uncertainty is calculated from the standard deviation of the repeated measurements (N) at the same locations and flow conditions. For example, the wall pressure measurements include 54 repeated runs at 32 distinct streamwise locations. The unbiased standard deviation, s, of a given quantity, X, can be found from:

$$s = \left[\frac{1}{N-1} \sum_{i=1}^{N} \left(X_i - \bar{X} \right)^2 \right]^{0.5} \tag{2}$$

where i is the index associated with the number of repeated measurements and $\bar{X}$ is the mean of the measurements.

For a 95% confidence interval, the random uncertainty is then given by

$$\delta_{rand} = t_{1-\frac{\alpha}{2}} \frac{s}{\sqrt{N}} \tag{3}$$

where $t_{1-\frac{\alpha}{2}}$ is the $1 - \frac{\alpha}{2}$ quantile of the t-distribution for N-1 degrees of freedom.

The instrumentation uncertainty for these measurements is obtained by combining the primary uncertainties from each measurement system and the associated sensitivity of the quantity of interest to these primary measurements, combined using a root sum square approach. For validating the as-built geometry of the empty test section, each individual test-section wall is considered unique, therefore the flow-field nonuniformity uncertainty cannot be estimated. For the purpose of validating the as-designed computations (that are assuming an idealized, square cross-section tunnel with four identical walls), uncertainties for the wall-averaged quantities were treated like random uncertainties (obtained from Eq. 2 and 3), where each wall is treated as a repeated realization. For example,

$$\bar{C} = \frac{1}{N} \sum_{i=1}^{N} \bar{X}_i \tag{4}$$

where $\bar{X}_i$ is an averaged quantity from wall i, and $\bar{C}$ is the wall-averaged data across N walls.

The uncertainty is then determined by Eq. 2 and 3. However, when the number of walls is 2 or less, the t-distribution cannot be used. Instead, the uncertainty is then obtained by combining the uncertainties of each wall together in a root sum squared fashion show in Eq. 5.

$$\delta_{total} = \sqrt{(\sum_{i=1}^{N} \delta_i^2} \tag{5}$$

3.6 As-Built Geometry Extraction

As described above, covering the full physical volume of the highspeed leg of the circuit (a domain that is 16.7m long, 5.5m high, and 5.5m wide overall) required combining multiple scans performed with multiple CMMs. The geometry of the settling chamber

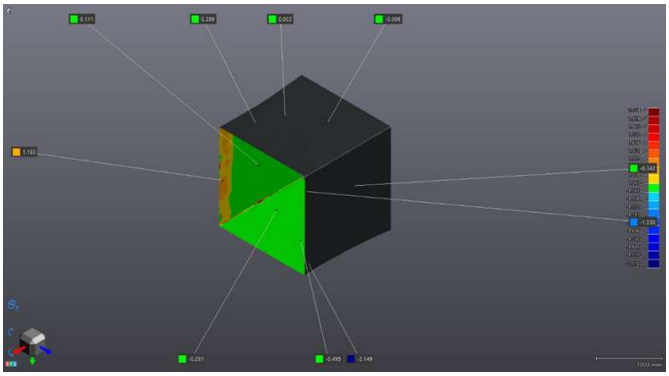


Fig. 15: Difference between the 2022 contraction liner and 2024 test-section scans over the last 1.8m of the contraction liner after alignment (units in mm).

and contraction (up to the start of the contraction liner) was extracted from a scan of the circuit performed in 2019 with a FARO Focus 3D CMM. The contraction liner and test-section geometry were obtained from scans performed with the Metrascan 3D CMM (in 2022 and 2024 respectively). All the point cloud processing was performed and programmed in MATLAB. Note that the coordinate system used in the scanned data presented here is different than the coordinate system used in the Roy et al. [4]. In the scanned data, the x-coordinate is aligned streamwise but has its origin at the end of the test-section (which is physically identifiable in the scan).

3.6.1 Scan Alignment

Each scan consists of a point cloud based in its own coordinate system. Combining the 3 point-clouds therefore implied aligning all 3 data sets to one coordinate system. The alignment of the contraction liner and test-section scans was performed in the native CREAFORM software platform VX Elements. The alignment was based on the overlapping region between the 2 scans (1.2m of the last 1.8m of the 4.1m-long contraction liner). Fig. 15 shows the difference between the contraction liner scan and the test-section scan over the 1.8m region of overlap once the two scans were referenced to each other and the alignment was performed. In this image, the flow direction is from right to left, and the deviations on the port and floor walls are visible. As seen in Fig. 15, evidence of the impact of the sidewall mounting adjustments in late 2023 can be seen at the most downstream end of the contraction liner on the port wall (where the liner meets the test-section, on the left of Fig. 15) with deviations up to $\pm$2.15mm. Since it is believed that this deviation arose from additional stress placed on the liner panel connected to the test-section, the decision was made to remove the very last 0.6m of the overlap region (corresponding to the last row of liner panels) from the alignment procedure. Consequently, it can be seen that outside this region, the final alignment yields agreement that are within $\pm$0.5mm.

3.6.2 Cross-Sectional Processing

Once all the scans are aligned and expressed in the same coordinate system, the point cloud information is processed to extract the tunnel geometry. The first step consists in extracting streamwise slices of the point cloud domain every 5mm. To obtain this information, the point cloud database is extracted over 5mm on either side of a given streamwise location. These cross-sectional data sets are then broken down by walls and processed to filter out noise from the signal. This is performed in 2 steps:

- Recursive Peak Elimination: unrealistic sudden variations in the wall geometry (where prominence of the peaks is greater than 8mm) are removed.
- Noise Rejection: increased variations due to optical reflections (occurring particularly on highly reflective aluminium foil tape found in the contraction liner and at the start of the test-section) is removed by rejecting points are more than ±4mm from the mean wall location. This value was selected as twice the typical uncertainty of the FARO Focus 3D CMM to ensure only points with significant noise would be removed.

A decision was then made regarding the level of fidelity of the corner geometry. As discussed in 2.1, fully capturing the fillets (in the corner of the contraction liner, Fig. 2) and gaskets (in the corners of the test-section, Fig. 4) in the CFD meshes would be very expensive computationally and could lead to iterative convergence issues. Therefore, it was decided that corner geometry should initially be idealized to a sharp corner which would ensure ease of meshing and simulation convergence. To do so, linear fits of the last 1/16 of two adjoining walls are computed, and the location of the idealized corner is set at their intersection. The idealized corner points are then linearly interpolated between the new corner and the point cloud data until the interpolated points are within a certain tolerance of the point cloud (to ensure a smooth transition between the idealized corner and the real geometry). This tolerance was set to 0.05mm in the contraction liner and test-section, and had to be increased to 0.25mm in the settling chamber and contraction, due to the coarser data there.

Once the sharp corners have been added to the geometry, the resulting point cloud is then bin-averaged over 2mm along each wall and finally linearly interpolated to 900 points per wall. The final linear interpolation allows the generation of a regular grid with a spanwise resolution of approximately 6mm in the settling chamber, and 2mm in the test-section.

All scan results (shown in 3.6.2 and 3.6.3) are presented in the original scan coordinate system where x_s is streamwise (positive towards turn 1), y_s is vertical (positive towards the ceiling), and z_s is horizontal (positive toward the port wall). The coordinate system is referenced at the bottom-port corner of the exit plane of the test-section (that was visually identifiable in the scan).

The outcome of the cross-section processing is illustrated at x_s = -12,000mm (as a representative sample of the FARO Focus 3D scan data in the contraction) in Fig. 16 and x_s = -6,000mm (as a sample of the Metrascan data in the test-section) in Fig. 17. In these figures, the 2D projection of the full domain is shown at the center in the red shaded area (part e), and the streamwise location where the comparison is presented is indicated by a black vertical line. The other 4 plots present the comparisons of

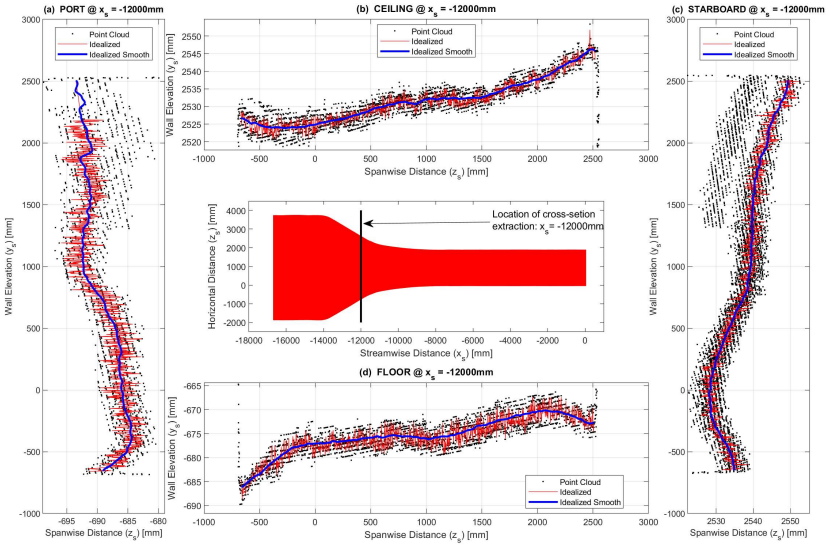


Fig. 16: Sample results of the idealized cross-sectional processing in the contraction (x_s = -12,000mm). Point cloud (black dots) are plotted against the idealized geometry (red line) and Gaussian smooth data (blue line) for the 4 walls in parts a-d. Part e presents the two-dimensional projection of the full domain and the location where the profiles were extracted is indicated as a black solid line.

the point cloud information (black dots) and the output of the idealized cross-section processing (in red line). Note that the scales on the axes are all different to reveal the finer variations in the data, and that the smooth data also provided as the blue lines in parts a-d will be discussed in 3.6.3. The noise reduction resulting from the cross-sectional processing is clear in Fig. 16, particularly on the port and starboard walls. The increased noise levels in the point cloud up and away from the scanner (mentioned in 2) are also clear in Fig. 16(a) and (c). The striking difference with the data in the test-section is also quite clear in Fig. 17 where, at the scale shown, the difference between the original (clean) point cloud and the cross-sectional data is undiscernible.

3.6.3 Gaussian Smoothing

As seen in Fig. 16 and Fig. 17, the cross-sectional processing results in a wall geometry that appears smooth in the test-section (compared to the scale of the physical variations due to panel bending or the edges of the paneling). However, closer inspection reveals the presence of sudden, point-to-point variations. These variations are even more marked in regions of higher curvature (like the contraction liner) or in the settling chamber (where despite the recursive peak elimination and noise rejection, noticeable point to point variation, up to 4mm, is present). These variations in turn

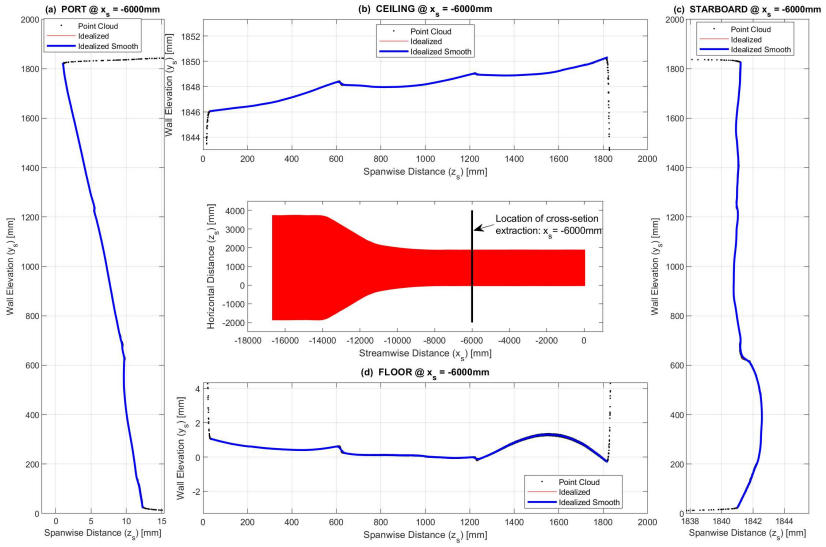


Fig. 17: Sample results of the idealized cross-sectional processing in the contraction (x_s = -6,000mm). Point cloud (black dots) are plotted against the idealized geometry (red line) and Gaussian smooth data (blue line) for the 4 walls in parts a-d. Part e presents the two-dimensional projection of the full domain and the location where the profiles were extracted is indicated as a black solid line.

lead to sudden slope changes that are not compatible with efficient meshing or simulation. It was therefore decided to apply a smoothing process to the cross-section data. This in itself provided a significant challenge as a balance needed to be found between over-smoothing (where geometric information would be lost but meshing would be simplified) and under-smoothing (where geometric information is retained, but meshing is more challenging). A Gaussian kernel smoothing was selected as this process ensures continuity in the data, does not produce artifacts, and is computationally very efficient at reducing noise. Several iterations of this smoothing were implemented to quantify the trade-off between geometric fidelity and meshing ability.

The magnitude of the Gaussian kernel smoothing is indeed controlled by a single parameter, the standard deviation σ that determines the physical extent of the Gaussian kernel, and hence how much of the data sets is included in the smoothing at any given point in space. The kernel G_σ is defined as:

$$G_\sigma = \frac{1}{2\pi\sigma^2} e^{-\frac{{x_w}^2+{y_w}^2}{2\sigma^2}} \tag{6}$$

where x_w and y_w are the streamwise and spanwise indices for each wall.

The kernel is then applied to each wall cross-sectional data set through two-dimensional convolution. The kernel size R_{G_σ}, the range over which the kernel is applied, is then selected as follows:

$$R_{G_\sigma} = 2\,[3\sigma] + 1 \tag{7}$$

After multiple evaluations of the impact of the smoothing, a standard deviation of 6 was ultimately selected to provide adequate smoothing while retaining important information like panel edge locations and panel bowing. Evaluation of the smoothing was done in two ways. First, the smooth geometry was compared to the original point cloud and the idealized cross-sectional data at several streamwise locations through the domain (in the settling chamber, the contraction, contraction liner, and in the test-section). An example of such comparison is shown in Fig. 16 and Fig. 17 for a streamwise location in the contraction and test-section respectively. As discussed earlier, the large amount of noise (and the efficacy of the peak elimination and noise filtering) in the FARO Focus 3D data is readily observable in Fig. 16 when comparing the black point cloud data and the red cross-section curve. The smoothing (blue line) in turn shows physically accurate bulk variations of the wall geometry without the high frequency noise present in the idealized data. Conversely, the data shown in the test-section (Fig. 17) reveal significantly less noise and very high fidelity in capturing small features like the transition between the test-section panelling or the bowing of some of the aluminium panels.

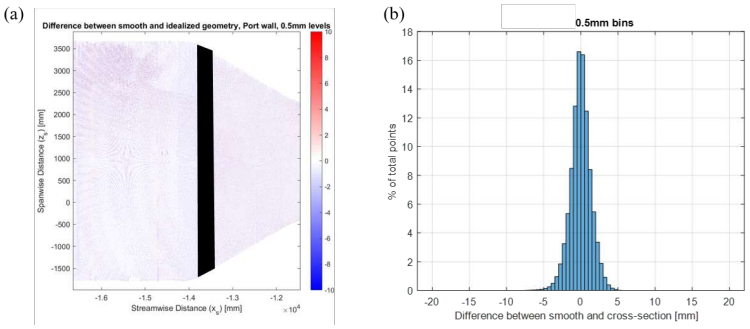


Fig. 18: Impact of Gaussian smoothing on the port wall geometry in the settling chamber and contraction: (a) contours of the difference in wall shape between the smooth data and the idealized cross-sectional data, and (b) histogram of the difference between smooth and idealized cross-sectional data.

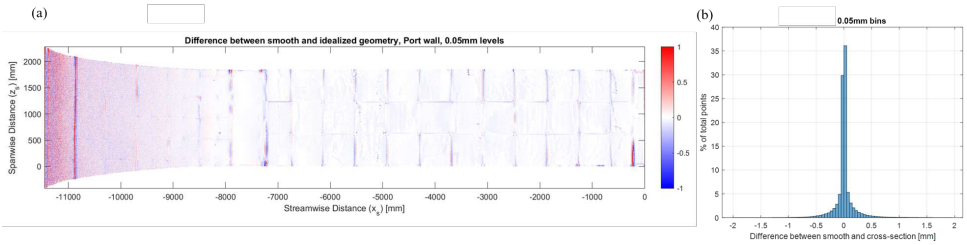


Fig. 19: Impact of Gaussian smoothing on the port wall geometry in the contraction liner and test-section: (a) contours of the difference in wall shape between the smooth data and the idealized cross-sectional data, and (b) histogram of the difference between smooth and idealized cross-sectional data.

Next, the impact of the smoothing is quantitatively assessed by computing the difference between the idealized cross-sectional and the smooth data sets over each wall. To analyze this information, the difference between the smooth geometry and the idealized geometry is plotted as a contour plot, and the histogram of the difference over the entire region is generated (see parts a and b in Fig. 18 and Fig. 19 for the port wall). Note that due to the different noise levels in the upstream point cloud (settling chamber + contraction) and downstream data set (contraction liner + test-section), the histogram bin size and the contour levels and maxima are different in Fig. 18 (0.5mm increments and ±10mm range) and Fig. 19 (0.05mm and ±1mm range) to reveal finer variations in the test-section. It should be noted that the presence in Fig. 18 of a black region around x_s = -13,500mm is due to a region of low scan resolution. This region could not be passed through the cross-sectional processing and is therefore not included in this comparison. Once all geometries are combined into one, data is linearly interpolated over this gap. Further inspection of Fig. 18 reveals that the Gaussian smoothing results in differences that are primarily within ±5mm for over 99% of the points (over 95% within ±2.8mm) of the cross-sectional data.

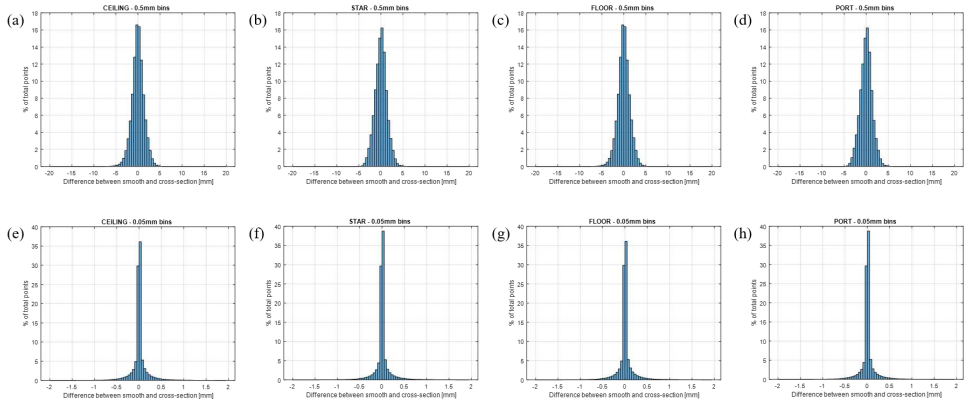


Fig. 20: Histograms of the difference between the smooth and idealized cross-sectional geometry for all 4 walls (a)-(d) in the settling chamber and contraction, and (e)-(h) in the contraction liner and test-section

On the other hand, in Fig. 19, the smoothing in the test-section results in differences that are within ±1mm for 99% of the points in the domain (and 95% within ±0.5mm). The histograms of the difference between smooth and idealized data for all 4 walls are provided in Fig. 20. Figure 20 shows that the impact of the smoothing is consistent on all four walls, with larger impact on the FARO Focus 3D data (with lower resolutions used in the settling chamber and upstream part of the contraction) than on the Metrascan data (used in the downstream part of the contraction and the test-section).

The final step to confirm the smoothing has not removed valuable geometric information is to inspect the mean curvature. This is most efficiently done in the contraction liner and test-section where the wall paneling leads to distinct features (like the edges and shape of each panel) that must be properly captured to ensure high fidelity of the CFD meshes.

An example of such analysis is shown in Fig. 21. In part c), the mean curvature is presented for the entire wall (here the port) as a contour plot in which 3 sections have been labeled:

- the spanwise variation of the wall shape at x_s=-9385mm (half way into the contraction liner) is shown in part a
- the spanwise variation of the wall shape at x_s=-5220mm (approximately 2m downstream of the test-section inlet) is shown in part b
- the streamwise variation of the wall shape at midspan is shown in part d.

It should be noted that the scales on the vertical and horizontal axes of parts a, b, and d are different to highlight the fine details of the geometries. Moreover, the contraction liner is not included in the plot in part c as the large change in elevation there (over 400mm from the inlet of the liner to its outlet) would render the small variation in the test-section invisible if they were plotted on the same scale. Fig. 21c shows that in the contraction and test-section, it is still possible to assess the presence of the

panelling (as evident in the grid pattern seen in the contours). Fig. 21a, b, and d also show that while sharp variations have been significantly smoothed out (like the noise at x_s=-9385mm in Fig. 21(a) or the panel discontinuities at 600 and 1210mm in Fig. 21b, the presence of the aluminium panels (and their shape) is very much retained throughout the whole domain.

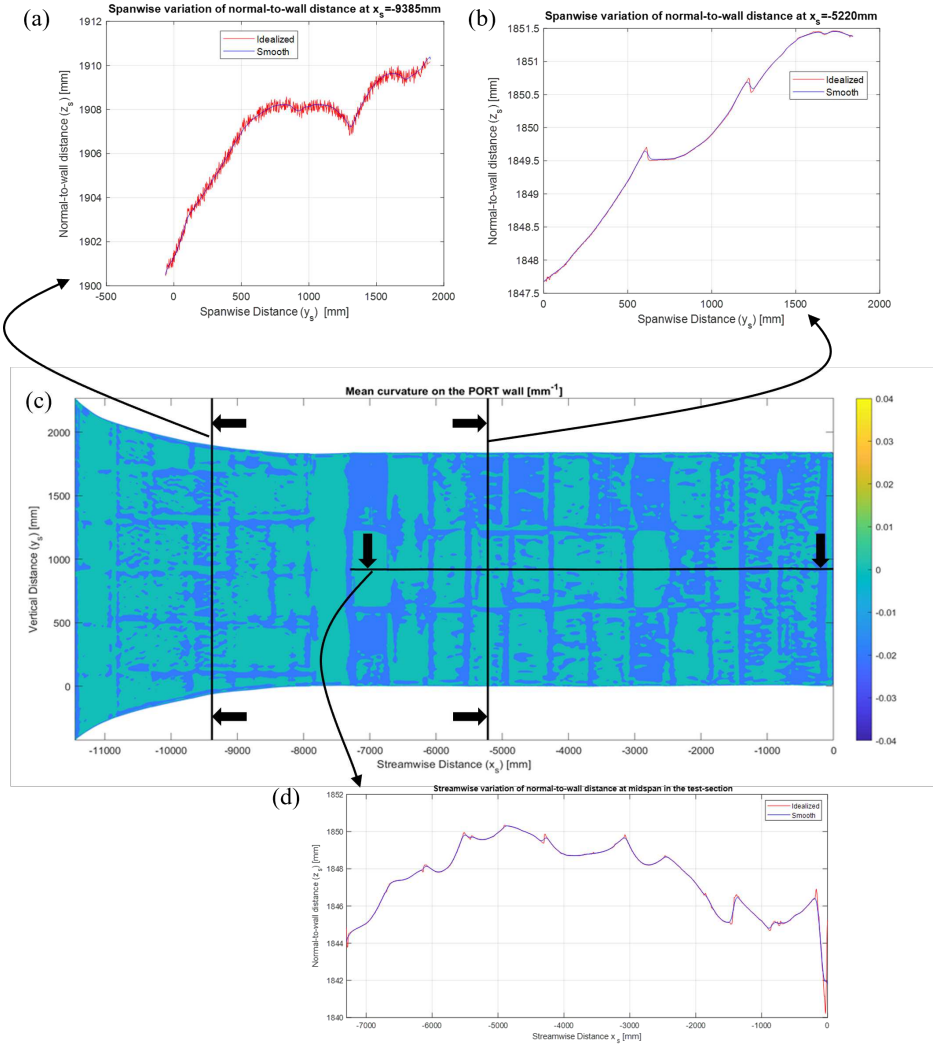


Fig. 21: Validation of smoothing process on captured wind tunnel geometry (port wall only): (a) Spanwise variation of normal-to-wall distance at x_s=-9385mm, (b) Spanwise variation of normal-to-wall distance at x_s=-5220mm, (c) contours of the mean curvature of the port wall, and (d) streamwise variation of the normal-to-wall distance at the midspan of the port wall.

4 Best Practices

The AVT-387 activities at the VTSWT have focused so far on characterizing (and modelling) the empty test-section flow. Despite the apparent simplicity of the problem, the task has proven challenging, and in the process, has revealed several important lessons that the authors would like to share below if one is to successfully characterize experimental boundary conditions in low-speed wind tunnels.

- Correction of any large scale non-nominal test section features (such as significant wall misalignment), is a critical pre-requisite of facility characterization for needed for CFD validation. Similarly, implementing modifications or installing instrumentation to ensure that quantities of significance to CFD boundary conditions are being documented, such as test-section bleed rate, is also key. Significance in this context can be judged by the likely magnitude of the deviation or un-documented condition on the core flow, as compared to measurement uncertainties for quantities to be directly used for CFD validation.
- Experimental techniques using simpler instrumentation over larger area or volume (like mean pressure over entire walls of the facility) are preferable over higher complexity more localized techniques when it comes to characterizing boundary conditions as they provide a wider basis of comparison with simulation. In turn, this enables the identification of local features (like the impact of wall paneling on the test-section wall distribution) as well as more global quantities (like the streamwise pressure gradient in the test-section) that in turn can serve as bases of validation for the CFD simulations.
- Measurements of the inflow is critical to fully capture variations in test-section flow behaviors (both in the corners and in the core). Obtaining measurements of the full inflow in the settling chamber is preferable as larger physical scales there allows for better definition of flow features. If the settling chamber is not readily accessible, measurements should be performed at the entrance of the test-section to provide critical inlet boundary condition to the CFD simulation.
- To minimize numerical uncertainty when comparing experimental and CFD data, aerodynamic measurement quantities should be extracted from isentropic relations and include compressibility effects even for subsonic flows like at the VTSWT. The methods used to reduce and process experimental data should indeed be identical to the ones used in the computational results to eliminate any potential bias and enable assessment of sensitivities.
- Experimental reference conditions, usually a static pressure tap (or taps) upstream of the model location, should be clearly defined and matched as precisely as possible in the computations. Information of importance includes the exact physical location of the reference measurements (to be matched in the CFD), ensuring they are free of interference (either from local tunnel geometry, or from the model mounted in the test-section), and the steps through they are processed to result in the reference quantities like reference velocity, Reynolds number, and Mach number.
- Great care is required when optically scanning a facility to extract the as-built geometry (whether idealized or full fidelity). Regions of noise should be studied on-site during the scan and any attempt to eliminate the sources of noise should be

made during the scanning campaign. Minimizing the number of scanners used will minimize the efforts needed to align all the different scans together, thus reducing uncertainties.
- Detailed documentation and clear referencing of coordinate systems should be established early on to ensure compatibility with CFD meshes. References should be introduced in the geometries to ensure orientation match between the experimental data and the CFD computations and meshes.

In addition, initial work on the preparation for the first model-in case has also revealed the following best practices.

- The experimental test case needs to take into account constraints from both the facility/instrumentation and the simulation. Indeed, a strong test-case will enable efficient data capture during the testing campaign and efficient simulation. The model (and associated mounting hardware) geometry should be a simple, well-defined geometry that does not generate challenging flows (e.g. large regions of separated flow) so the simulation can focus on the interaction between model and facility rather than spending resources capturing a complex flow around the model.
- While on-model information (through techniques like surface pressure, force balance, infrared thermography, or flow visualization) will be important, the flow around the model will be just as important as the flow around the model mount, which consequently should be instrumented to better define the flow conditions there.

5 Conclusions

As part of the AVT-387 efforts to model the flow inside the Virginia Tech Stability Wind Tunnel, the experimental boundary conditions in the facility have been characterized in great details. In particular, the inflow in the settling chamber was measured over the full cross-section downstream of the last turbulence screen (5.5m×5.5m) and showed good uniformity. The mean surface pressure distribution on the 4 walls in the contraction liner (covering the latter half of the contraction) and the two side walls in the test-section has been documented, along with the boundary layer shape and growth across all 4 walls and along the entire test-section. The details of the corner flow at the reference location were revealed by stagnation pressure contours and have proven useful to evaluate the accuracy of the numerical simulations. Finally, the as-built geometry was extracted from multiple scans of the facility as an idealized cross-section data set, smooth enough to allow for efficient yet accurate CFD meshing, with sharp corners throughout the domain. Future efforts will focus on the preparation of the model-in test case. The actual model, in the form of the 2.5% scale NASA juncture flow model (a risk reduction model of the 8% model tested in the 14'x22' facility at Langley NASA Langley Research Center [7]), has been selected due to its simplicity and well documented testing history (including in the VTSWT).

Acknowledgments. The authors would like to acknowledge the support from the Office of Naval Research, in particular Dr. Julie Young, for their contribution on this research under research grant number N00014-22-1-2660. Also, special thanks to Dr.

Máté Szőke, Bill Oetjens, the wind tunnel engineer, James Lambert, Cameron Hollandsworth, Roy Handy, Randall Monk and Scott Patrick from the AOE machine shop for their continuous and tremendous support. We would also like to acknowledge the contribution of undergraduate researchers in particular Rujipa Shayutapong, Jaedyn Williams, ThanhLong Duong, Maiann Borgoltz and Kevin Xu, as well as the students in the Spring 2023 and 2024 offering of AOE3054 – Experimental Methods for assisting with the acquisition of part of the data set used in this investigation.

Declarations

Funding. This work was supported by the US Office of Naval Research (ONR award N00014-22-1-2660).

Conflict of interest. The authors declare that they have no conflict of interest.

References

[1] Vishwanathan, V., Szoke, M., Duetsch-Patel, J.E., Gargiulo, A., Fritsch, D.J., Borgoltz, A., Roy, C.J., Lowe, K.T., Devenport, W.J.: Aerodynamic design and validation of a contraction profile for flow field improvement and uncertainty quantification in a subsonic wind tunnel. In: AIAA SciTech Forum, Orlando, FL (2020)

[2] Intaratep, N., Szoke, M., Borgoltz, A., Devenport, W., Shayutapong, R., Williams, J., Duong, T.: Detailed investigation of the boundary layer development on large scale subsonic wind tunnel walls for numerical validation. In: AIAA SciTech Forum, Orlando, FL (2024)

[3] Borgoltz, A., Intaratep, N., Devenport, W., Roy, C., HogePatil, A., Dixon, M.: VT Stability Tunnel: Experimental characterization of boundary conditions for subsonic wind tunnels. In: AIAA AVIATION Forum 2026, Diego, CA (2026)

[4] HogePatil, A., Roy, C.J., Borgoltz, A., Intaratep, N., Devenport, W., Forsyth, P., Di Pasquale, D., Józsa, T., Lilly, A.A., Kurtulus, D.F., Anilir, B., Kuenn, A., Elmiligui, A., Carlson, J.-R., Rumsey, C., Erturk, B., Ozcetin, M.H.: Computational fluid dynamics comparisons for the Virginia Tech Stability Wind Tunnel. CEAS Aeronautical Journal (2026). In preparation for publication

[5] Rhode, M.N., Oberkampf, W.L.: Estimation of uncertainties for a model validation experiment in a wind tunnel. Journal of Spacecraft and Rockets **54**(1) (2017)

[6] Duetsch-Patel, J.: Structure and turbulence of the three-dimensional boundary layer flow over a hill. PhD thesis, Virginia Tech (2023)

[7] NASA Langley Research Center: Exp: NASA Juncture Flow (JF). Last accessed 31 January 2025 (2025). https://turbmodels.larc.nasa.gov/Other_exp_Data/junctureflow_exp.html